The connection between mass and light in galaxy clusters

Sifón Andalaft, C.J.

6 | The galaxy-subhalo connection in low-redshift galaxy clusters from weak gravitational lensing

We measure the gravitational lensing signal around satellite galaxies in galaxy clusters at $z < 0.15$ by combining high-quality imaging data from the Canada-France-Hawaii Telescope with a large sample of spectroscopically-confirmed cluster members. We use extensive image simulations to assess the accuracy of shape measurements of faint, background sources in the vicinity of bright satellite galaxies. We find a small but significant bias, as light from the lenses makes the shapes of backgroud galaxies appear more radial than they really are. We account for this bias by applying a correction that depends on both lens size and magnitude. We also determine and apply a scale-dependent boost factor to account for contamination of the source sample by cluster members. We measure the satellite lensing signal robustly down to scales of roughly 30 kpc, but we cannot constrain the matter density profiles of subhaloes. We estimate the subhalo mass as the mass bound to the subhalo, consistent with the definition of common subhalo finders, and provide a direct measurement of the subhalo-to-stellar-mass relation, $\log m_{\rm bg}/{\rm M}_\odot = (11.73 \pm 0.05) + (0.77 \pm 0.11) \log[m_\star/(2 \times 10^{10}\,{\rm M}_\odot)]$, broadly consistent with the corresponding relation for central galaxies. The slope of this relation is robust to both the adopted mass-concentration relation and the definition of subhalo mass. We also constrain the mass segregation of subhaloes by measuring the lensing signal as a function of projected cluster-centric distance. We find no statistically significant evidence for mass segregation, in qualitative agreement with predictions from numerical simulations.

Cristóbal Sifón, Ricardo Herbonnet, Henk Hoekstra, et al.,
in preparation

6.1. Introduction

According to the hierarchical structure formation paradigm, galaxy clusters grow by the continuous accretion of smaller galaxy groups and individual galaxies. Initially, each of these systems is hosted by their own dark matter halo, but as a galaxy falls into a larger structure, tidal interactions transfer mass from the infalling galaxy into the new host. The galaxy then becomes a satellite and its dark matter halo, a subhalo.

Detailed studies on the statistics of subhaloes from numerical N-body simulations have revealed that subhaloes are severely affected by their host haloes. Dynamical friction makes more massive subhaloes sink towards the centre faster, while tidal stripping removes mass preferentially from the outskirts of massive subhaloes closer to the centre. These two effects combined destroy the most massive subhaloes soon after infall (e.g., Tormen et al. 1998; Taffoni et al. 2003), a result exaggerated in simulations with limited resolution (e.g., Klypin et al. 1999; Taylor & Babul 2005; Han et al. 2016). Tidal stripping makes subhaloes more concentrated than field haloes of the same mass (e.g., Ghigna et al. 1998; Springel et al. 2008; Moliné et al. 2016), and counterbalances the spatial segregation induced by dynamical friction (van den Bosch et al. 2016).

One of the most fundamental questions is how these subhaloes are linked to the satellite galaxies they host, which are what we can observe in the real Universe. Taking N-body simulations at face value results in serious inconsistencies with observations, the most famous of which are known as the "missing satellites" (Klypin et al. 1999; Moore et al. 1999) and "too big to fail" (Boylan-Kolchin et al. 2011) problems. It has since become clear that these problems may arise because baryonic physics has a strong influence on the small-scale distribution of matter. Energetic feedback from supernovae at the low-mass end, and active galactic nuclei at the high-mass end, of the galaxy population affect the ability of dark matter (sub)haloes to form stars and retain them. In addition, the excess mass in the centre of galaxies (compared to dark matter-only simulations) can modify each subhalo's susceptibility to tidal stripping (e.g., Zolotov et al. 2012).

Despite these difficulties, given the current technical challenges of generating cosmological high-resolution hydrodynamical simulations (in which galaxies form self-consistently), N-body simulations remain a valuable tool to try to understand the evolution of galaxies and (sub)haloes. In order for them to be applied to real observations, however, one must post-process these simulations in some way that relates subhaloes to galaxies, taking into account the aforementioned complexities (and others). For instance, semi-analytic models contain either physical or phenomenological recipes whether or not to form galaxies in certain dark matter haloes based on the mass and assembly history of haloes (e.g., Bower et al. 2006; Lacey et al. 2015). A different method involves halo occupation distributions (HODs), which assume that the average number of galaxies in a halo depends only on host halo mass. Because they provide an analytical framework to connect galaxies and dark matter haloes, HODs are commonly used to interpret galaxy-galaxy lensing and galaxy clustering measurements through a conditional stellar mass (or luminosity) function (e.g., Seljak 2000; Peacock & Smith 2000; Mandelbaum et al. 2006b; Cacciato et al. 2009; van den Bosch et al. 2013).

One of the key aspects of these prescriptions is the stellar-to-halo mass relation. While many studies have constrained the stellar-to-halo mass relation of central galaxies (e.g.,

Hoekstra et al. 2005; Heymans et al. 2006b; Mandelbaum et al. 2006b, 2016; More et al. 2011; van Uitert et al. 2011, 2016; Leauthaud et al. 2012; Velander et al. 2014), this is not the case for satellite galaxies, whose stellar-to-*sub*halo mass relation (SHSMR) remains essentially unexplored, and the constraints so far are limited to indirect measurements. Rodríguez-Puebla et al. (2012) used abundance matching (the assumption that galaxies rank-ordered by stellar mass can be uniquely mapped to [sub]haloes rank-ordered by total mass) to infer the SHSMR using the satellite galaxy stellar mass function, and Rodríguez-Puebla et al. (2013) extended these results using galaxy clustering measurements. They showed that the SHSMR is significantly different from the central stellar-to-total mass relation, and that assuming an average relation when studying a mixed population can lead to biased results (see also Yang et al. 2009).

Instead, only stellar dynamics and weak gravitational lensing provide direct ways to probe the total gravitational potential of a galaxy. However, the quantitative connection between stellar velocity dispersion and halo mass is not straightforward (e.g., Li et al. 2013b; Old et al. 2015), and only weak lensing provides a direct measurement of the total surface mass density (Fahlman et al. 1994; Clowe et al. 1998). Using deep Hubble Space Telescope (HST) observations, Natarajan et al. (1998, 2002, 2007, 2009) measured the weak (and also sometimes strong) lensing signal of galaxies in six clusters at $z = 0.2 - 0.6$. After fitting a truncated density profile to the ensemble signal using a maximum likelihood approach, they concluded that galaxies in clusters are strongly truncated with respect to field galaxies. Using data for clusters at $z \sim 0.2$ observed with the CFH12k instrument on the Canada-Hawaii-France Telescope (CFHT), Limousin et al. (2007) arrived at a similar conclusion. Halkola et al. (2007) and Suyu & Halkola (2010) used strong lensing measurements of a single cluster and a small galaxy group, respectively, and also found evidence for strong truncation of the density profiles of satellite galaxies. However, Pastor Mira et al. (2011) have argued that the conclusion that cluster galaxies are truncated from these (strong and weak) galaxy-galaxy lensing measurements are driven by the parametrization of the galaxy density profiles rather than constraints from the data themselves.

Recent combinations of large weak lensing surveys with high-purity galaxy group catalogues have allowed direct measurements of the average subhalo masses associated with satellite galaxies using weak galaxy-galaxy lensing (Li et al. 2014, 2016, **Chapter 5**). However, these studies did not focus on the SHSMR but on the segregation of subhaloes by mass within galaxy groups, by measuring subhalo masses at different group-centric distances. The observational results are consistent, within their large errorbars, with the mild segregation seen in numerical simulations and semi-analytic models (Han et al. 2016; van den Bosch et al. 2016).

In this work, we present weak gravitational lensing measurements of the total mass of satellite galaxies in 50 massive galaxy clusters at $z < 0.15$. Our images were taken with the MegaCam instrument on CFHT, which provides a larger field of view (1 sq. deg.) than CFH12k. This large field of view allows us to focus on very low redshift clusters and take advantage of the $< 1''$ seeing (corresponding to 1.84 kpc at $z = 0.1$) of our observations. We can therefore probe the lensing signal close to the galaxies themselves, at a physical scale equivalent to what can be probed in a cluster at $z \sim 0.5$ with HST, but out to the clusters' virial radii. In addition, the low-redshift clusters we use have extensive spectroscopic observations available from various data sets, compiled in **Chapter 4**, so we do not need to

rely on uncertain photometric identification of cluster members.

This chapter is organized as follows. We summarize the galaxy-galaxy lensing formalism in Section 6.2. We describe our data set in Section 6.3, taking a close look at the source catalogue and the shapes of background sources in Section 6.4. We present our modelling of the satellite lensing signal in Section 6.5, and discuss the connection between mass and light in satellite galaxies in Section 6.6.

We adopt a flat Λ cold dark matter (ΛCDM) cosmology with $\Omega_\mathrm{m} = 0.315$, based on the latest results from cosmic microwave background observations by Planck Collaboration (2015a), and $H_0 = 70\,\mathrm{km\,s^{-1}Mpc^{-1}}$. In this cosmology, $10'' = \{9.8, 18.4, 26.1\}\,\mathrm{kpc}$ at $z = \{0.05, 0.1, 0.15\}$. As usual, stellar and (sub)halo masses depend on the Hubble constant as $m_\star \sim 1/H_0^2$ and $m \sim 1/H_0$, respectively.

6.2. Weak galaxy-galaxy lensing

Gravitational lensing distorts the images of background ("source") galaxies as their light passes near a matter overdensity along the line-of-sight. This produces a distortion in the shape of the background source, called *shear*, and a *magnification* effect on the source's size (and consequently its brightness). Starting from a measurement of the shape of an object in a cartesian frame with components (γ_1, γ_2) (see Section 6.4.1), the shear can be computed as

$$\begin{pmatrix} \gamma_\mathrm{t} \\ \gamma_\times \end{pmatrix} = \begin{pmatrix} -\cos 2\phi & -\sin 2\phi \\ \sin 2\phi & -\cos 2\phi \end{pmatrix} \begin{pmatrix} \gamma_1 \\ \gamma_2 \end{pmatrix}, \tag{6.1}$$

where ϕ is the azimuthal angle of the lens-source vector, γ_t measures the ellipticity in the tangential ($\gamma_\mathrm{t} > 0$) and radial ($\gamma_\mathrm{t} < 0$) directions and $\gamma_\times$ measures the ellipticity in directions 45° from the tangent. Because of parity symmetry, we expect $\langle \gamma_\times \rangle = 0$ for an ensemble of lenses (Schneider 2003) and therefore $\gamma_\times$ serves as a test for systematic effects.

The shear is related to the excess surface mass density (ESD), $\Delta\Sigma$, via

$$\Delta\Sigma(R) \equiv \bar{\Sigma}(< R) - \bar{\Sigma}(R) = \gamma_\mathrm{t} \Sigma_\mathrm{c}, \tag{6.2}$$

where $\bar{\Sigma}(< R)$ and $\bar{\Sigma}(R)$ are the average surface mass density within a radius[1] R and within a thin annulus at distance R from the lens. The critical surface density, Σ_c, is a geometrical factor that accounts for the lensing efficiency,

$$\Sigma_\mathrm{c} = \frac{c^2}{4\pi G} \frac{D_\mathrm{s}}{D_\mathrm{l} D_\mathrm{ls}}, \tag{6.3}$$

where, D_l, D_s, and D_ls are the angular diameter distances to the lens, to the source and between the lens and the source, respectively. The ESD for each bin in lens-source separation is then

$$\Delta\Sigma = \Sigma_\mathrm{c} \frac{\sum_i w_i \gamma_{\mathrm{t},i}}{\sum_i w_i}, \tag{6.4}$$

[1] As a convention, we denote three-dimensional distances with lower case r and two-dimensional distances (that is, projected on the sky) with upper case R.

where the sums run over all lens-source pairs in a given bin and the weight of each source galaxy is given by

$$w_i = \frac{1}{\langle \epsilon_{\rm int}^2 \rangle + (\sigma_{\gamma,i})^2}. \tag{6.5}$$

Here, σ_γ is the measurement uncertainty in $\gamma_{\rm t}$ due to shot noise in the images (see Section 6.4.1). We set the intrinsic root-mean-square galaxy ellipticity, $\langle \epsilon_{\rm int}^2 \rangle^{1/2}$, to 0.25.

In fact, the weak lensing observable is the *reduced* shear, $g \equiv \gamma/(1-\kappa)$ (where $\kappa = \Sigma/\Sigma_{\rm c}$ is the lensing convergence), but in the weak limit $\kappa \ll 1$ so that $g \approx \gamma$. However, close to the centres of galaxy clusters the convergence is of order unity, so this approximation is not accurate anymore. To account for this, the lensing model presented in Section 6.5 is corrected using

$$g(R) = \frac{\gamma(R)}{1 - \bar{\Sigma}(R)/\Sigma_{\rm c}} = \frac{\Delta\Sigma(R)/\Sigma_{\rm c}}{1 - \bar{\Sigma}(R)/\Sigma_{\rm c}}. \tag{6.6}$$

6.2.1. Statistical errors: data covariance

Because the gravitational potential of satellites in a cluster is traced by the same background source galaxies, data points in the ESD are correlated. Following Viola et al. (2015), we can re-arrange Equation 6.4 to reflect the contribution from each *source* galaxy. The data covariance can then be written as

$$\mathbf{Cov}_{mnij} = \langle \epsilon^2 \rangle^{1/2} \frac{\sum_s \left(C_{si,m} C_{sj,n} + S_{si,m} S_{sj,n} \right)}{\left(\sum_s Z_{si,m} \right) \left(\sum_s Z_{sj,n} \right)}, \tag{6.7}$$

where index pairs m, n and i, j run over the observable bins (e.g., stellar mass) and lens-source separation, R, respectively, and C, S and Z are sums over the lenses:

$$\begin{aligned} C_{si} &= -\sum_l w_{ls} \Sigma_{{\rm c},ls}^{-1} \cos 2\phi_{ls}, \\ S_{si} &= -\sum_l w_{ls} \Sigma_{{\rm c},ls}^{-1} \sin 2\phi_{ls}, \\ Z_{si} &= \sum_l w_{ls} \Sigma_{{\rm c},ls}^{-2}, \end{aligned} \tag{6.8}$$

and we assume zero covariance between clusters. In Equations 6.7 and 6.8, we explicitly allow for the possibility that the source weight, w, may be different for each lens-source pair (as opposed to a unique weight per source). This is the case when we consider the corrections to the shape measurements from lens contamination discussed in Section 6.4.1.

In addition to the data covariance there is, in principle, a contribution to the measurement uncertainty from sample variance. By comparing Equation 6.7 to uncertainties estimated by bootstrap resampling, in **Chapter 5** we showed that the contribution from sample variance is less than 10% for satelite galaxy-galaxy lensing measurements when limited to small lens-source separations ($R \lesssim 2$ Mpc).

6.3. Data set

In this section we describe the lens and source galaxy samples we use in our analysis. In the next section, we make a detailed assessment of the shape measurement and quality

cuts on the source sample using extensive image simulations.

6.3.1. Cluster and lens galaxy samples

The Multi-Epoch Nearby Cluster Survey (MENeaCS, Sand et al. 2012) is a targeted survey of 57 galaxy clusters in the redshift range $0.05 \lesssim z \lesssim 0.15$ observed in the g and r bands with MegaCam on the Canada-France-Hawaii Telescope (CFHT). The image processing is described in detail in van der Burg et al. (2013); all images have seeing $\lesssim 0.8''$. In **Chapter 4**, we compiled a large sample of spectroscopic redshift measurements in the direction of 46 of these clusters, identifying a total of 7945 spectroscopic members. Since, Rines et al. (2016) have published additional spectroscopic redshifts for galaxies in 12 MENeaCS clusters, six of which are included in **Chapter 4** but for which the observations of Rines et al. (2016) represent a significant increase in the number of member galaxies. We select cluster members in these 12 clusters in an identical way as in **Chapter 4**. From the member catalogue of **Chapter 4** we exclude all brightest cluster galaxies (BCGs), and refer to all other galaxies as satellites. Because the shapes of background galaxies near these members is very likely to be contaminated by light from the BCG, we also exclude all satellite galaxies within $10''$ of the BCGs to avoid severe contamination from extended light. Finally, we impose a luminosity limit $L_{\rm sat} < \min(2L^\star, 0.5L_{\rm BCG})$, where $L^\star(z)$ is the r-band luminosity corresponding to the characteristic magnitude, $m^\star_{\rm phot}(z)$ of the Schechter (1976) function, fit to red satellite galaxies in redMaPPer galaxy clusters over the redshift range $0.05 < z < 0.7$ (Rykoff et al. 2014).[2] We choose the maximum possible luminosity, $2L^\star$, because the BCGs in our sample have $L_{\rm BCG} \gtrsim 3L^\star$, so this ensures we do not include central galaxies of massive (sub)structures that could, for instance, have recently merged with the cluster. In addition, we only include satellites within 2 Mpc of the BCG. At larger distances, contamination by fore- and background galaxies becomes an increasingly larger problem. Our final spectroscopic sample consists of 5414 satellites in 51 clusters.

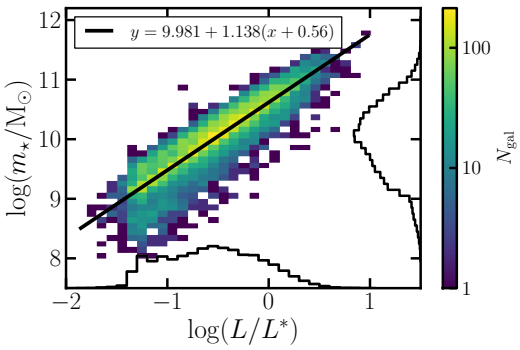

Figure 6.1: Relation between stellar mass and r-band luminosity for all satellites with stellar mass measurements. The color scale shows the two-dimensional histogram while the bottom and right histograms show the individual distributions. The black line is the best-fit relation, shown in the legend.

In addition, we include red sequence galaxies in all MENeaCS clusters in order to improve our statistics. We measure the red sequence by fitting a straight line to the colour-magnitude relation of red galaxies in each cluster using a maximum likelihood approach (C. Sifón et al., in prep.). Following the results of **Chapter 4**, we include only red sequence galaxies brighter than $M_{\rm r} = -19$ and within 1 Mpc of the BCG.[3] When we include

[2] Equation 9 of Rykoff et al. (2014) provides a fitting function for the i-band $m^\star_{\rm phot}(z)$, which we convert to r-band magnitudes assuming a quiescent spectrum, appropriate for the majority of our satellites, using EzGal (`http://www.baryons.org/ezgal/`, Mancone & Gonzalez 2012).

[3] Here, $M_{\rm r}$ is the $k+e$–corrected absolute magnitude in the r-band, calculated with EzGal using a pas-

red sequence galaxies, we also use the seven clusters without spectroscopic cluster members. Therefore our combined spectroscopic plus red sequence sample includes 9059 cluster members in 57 clusters. Throughout, we refer to the spectroscopic and spectroscopic plus red sequence samples as 'spec' and 'spec+RS', respectively.

Using u- and i-band data taken with either MegaCam or the Wide-Field Camera on the Isaac Newton Telescope in La Palma, van der Burg et al. (2015) estimated stellar masses for the 46 clusters with spectroscopic data from **Chapter 4**. Stellar masses were estimated by fitting each galaxy's spectral energy distribution using FAST (Kriek et al. 2009) assuming a Chabrier (2003) initial mass function. The only factor determining whether a particular galaxy has a stellar mass estimate or not is whether the cluster it resides in has u- and i-band data. We therefore regard the subsample of satellites with stellar masses as a representative subsample of our full catalogue. We therefore also include galaxies in clusters without stellar mass catalogues (corresponding to roughly 15% of the galaxies) by assigning stellar masses to them based on a fit to the stellar masses as a function of r-band luminosity, $L^\star$. For each galaxy, we assign its stellar mass from a normal distribution centred on this relation and with a spread given by the scatter in Figure 6.1. The relation we use is

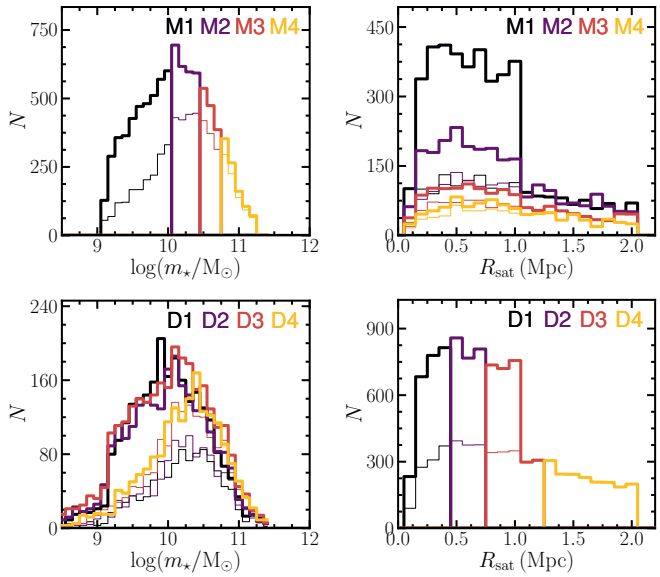

Figure 6.2: Stellar mass and cluster-centric distributions for the four bins in stellar mass used in Section 6.6.1 (top) and in cluster-centric distance used in Section 6.6.2 (bottom). Thin and thick histograms show the distributions of the spectroscopic and the spectroscopic-plus-red-sequence samples, respectively.

$$\log m_\star = (9.981 \pm 0.002) + (1.138 \pm 0.005)\left(\log L/L^* + 0.56\right), \tag{6.9}$$

and is shown in Figure 6.1. We have checked that the inclusion of galaxies without stellar masses through the above procedure does not bias any of our results.

In order to characterize the connection between satellite galaxies and their host subhaloes, we split the sample by stellar mass (Section 6.6.1) and cluster-centric distance (Section 6.6.2), each time splitting the sample in four bins. We show the stellar mass and cluster-centric distributions of the resulting subsamples in Figure 6.2, and list the average values in Table 6.1.

sively evolving Charlot & Bruzual (2007, unpublished, see Bruzual & Charlot 2003) model with formation redshift $z_{\rm f} = 5$.

6.3.2. Source galaxy sample

We construct the source catalogues in an identical manner to Hoekstra et al. (2015), except for one additional constraint discussed in Section 6.4. The biases in the shape measurements of the sources, depending on how the source sample is defined, have been characterized in great detail by Hoekstra et al. (2015). Although the study of Hoekstra et al. (2015) refers to a different cluster sample, both samples have been observed with the same instrument under very similar conditions of high image quality, so we can safely take the analysis of Hoekstra et al. (2015) as a reference for our study. Specifically, we select only sources with r-band magnitudes[4] $20 < m_{\rm phot} < 24.5$, with sizes $r_{\rm h} < 5$ pix and an additional constraint on $\delta m_{\rm phot}$, the difference in estimated magnitude before and after the local background subtraction (see Section 6.4). Compared to Hoekstra et al. (2015), who used $22 < m_{\rm phot} < 25$, we choose different limits at the bright end because our cluster sample is at lower redshift and therefore cluster members are brighter, and at the faint end because our data are slightly shallower, complicating the shape measurements of very faint sources.

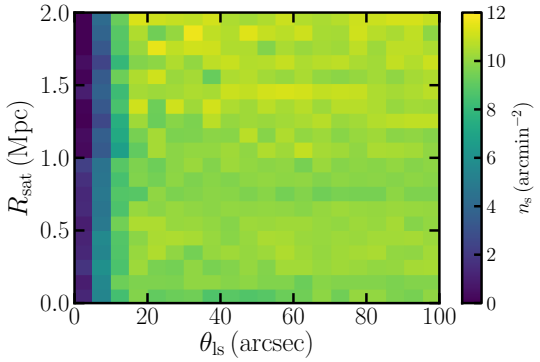

Figure 6.3: Observed number density of background sources as a function of lens-source separation, $\theta_{\rm ls}$, and distance from the lens to the cluster centre, $R_{\rm sat}$, for all 57 MENeaCS clusters, after applying all the cuts described in Section 6.3.

The source density after applying these cuts is $n_{\rm s} = 10.5$ arcmin^{-2}. Unlike most cluster lensing studies (e.g., Hoekstra et al. 2012; Applegate et al. 2014; Umetsu et al. 2014), we do not apply a colour cut to our source sample, since this only reduces contamination by ~30% (Hoekstra 2007). Instead, we follow Hoekstra et al. (2015) and correct for contamination in the source sample by applying a 'boost factor' to the measured lensing signal to account for the dilution by cluster members (e.g., Mandelbaum et al. 2005), defined here as

$$\mathscr{B}(\theta_{\rm ls}) = \frac{n_{\rm s,data}(\theta_{\rm ls})}{n_{\rm s,sim}(\theta_{\rm ls})} \frac{\langle n_{\rm s,sim}(\infty)\rangle}{\langle n_{\rm s,data}(\infty)\rangle}. \qquad (6.10)$$

We define $n_{\rm s}(\infty)$ as the number density as far as possible from the cluster, such that the measurement is contaminated by cluster members as least as possible. Because of the

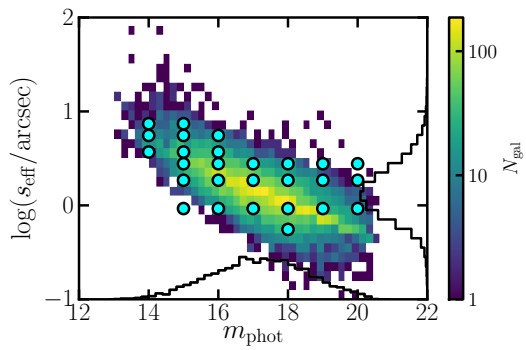

Figure 6.4: Magnitude and size distribution of satellites in the MENeaCS spec+RS sample. The logarithmic color scale shows the number of galaxies per two-dimensional bin, while black histograms show the one-dimensional distributions. Cyan circles show the coordinates used in the image simulations.

[4]We denote r-band magnitudes with $m_{\rm phot}$ in order to avoid confusion with subhalo masses, which we denote with lower case m and subscripts depending on the definition (see Section 6.5.2).

low redshift of our cluster sample, the field of view is sometimes not sufficient to probe a region truly devoid of cluster galaxies, but this has no impact on our results.

In the case of satellite galaxy-galaxy lensing there is a particularly high number density of lenses, which act as masks in our source sample in the regions where we most care about the signal—as close as possible to the lenses. In Figure 6.3, we show the source density as a function of both lens cluster-centric distance, $R_{\rm sat}$, and lens-source separation, $\theta_{\rm ls}$. The source density is fairly independent of both quantities, except for a sharp decrease at $\theta_{\rm ls} < 20''$, caused by the presence of cluster members which hide background sources (see Section 6.4.2). There is also a slight (~10%) decrease in $n_{\rm s}$ around lenses closer to the cluster centre, which can similarly be attributed to the higher lens density.

Roughly 20% of our satellites reside in clusters at $z < 0.06$, at which redshift the maximum distance from the centre within the 1 sq. deg. field of view of MegaCam (i.e., $30'$) corresponds to 2 Mpc. At larger radii the average signal may be biased since progressively fewer lenses from fewer clusters contribute to the measurements. We therefore only consider lens-source separations $R < 2\,\mathrm{Mpc}$ (where $R = D_A(z)\theta_{\rm ls}$) for our analysis.

6.4. Bias assessment and calibration through image simulations

In order to assess the impact of the lenses on our source sample (Section 6.4.2) and shape measurements (Section 6.4.1), we inject bright galaxies into the image simulations produced by Hoekstra et al. (2015). We place round galaxies modelled by Sérsic (1968) profiles with index $n = 4$ in a regular grid in the simulated images, separated at least $60''$ from each other. Figure 6.4 shows the distribution of magnitudes, $m_{\rm phot}$, and sizes, $s_{\rm eff}$, in the data, and the parameter space sampled with the simulations. The light profiles of the simulated lenses are truncated at $5 \times s_{\rm eff}$, where $s_{\rm eff}$ is the effective, or half-light, radius of the Sérsic profile. Galaxies are truncated to avoid confusion of light coming from different lenses, which would alter the inferred bias.

6.4.1. Shape measurements

To measure the galaxy-galaxy lensing signal we must be able to accurately infer the shear field around the lenses by measuring the shapes of as many background galaxies as possible. Most of these sources are faint and of sizes comparable to the image resolution, quantified by the point spread function (PSF). Blurring by the PSF leads to a multiplicative bias, μ, while an anisotropic PSF introduces an additive bias, c (e.g., Heymans et al. 2006a). The measured (or observed) shear is therefore related to the true shear by

$$\gamma^{\rm obs}(\theta) = \left(1 + \mu\right)\gamma^{\rm true}(\theta)\mathscr{B}^{-1}(\theta) + c\,. \tag{6.11}$$

Note that μ, c and $\mathscr{B}(\theta)$ depend on both the shape measurement method and the dataset on which the method is applied. As with any bias, it is not the magnitude of μ or c that is important but the accuracy with which it is known; this determines the accuracy to which they can be corrected for.

We measure galaxy shapes by calculating the moments of galaxy images using the KSB method (Kaiser et al. 1995; Luppino & Kaiser 1997), incorporating the modifications

by Hoekstra et al. (1998, 2000). Hoekstra et al. (2015) used extensive image simulations to assess the performance of KSB depending on the observing conditions and background source ellipticity, magnitude and size distributions. We adopt the size– and signal-to-noise–dependent multiplicative bias correction obtained by Hoekstra et al. (2015). Instead of correcting each source's measured shape, we apply an average correction to each data point, since the latter is more robust to uncertainties in the intrinsic ellipticity distribution (Hoekstra et al. 2015).

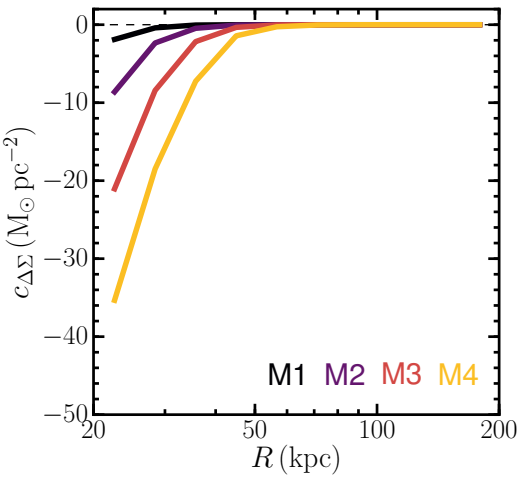

Figure 6.5: Average tangential additive bias, $c_{\Delta\Sigma} \equiv \Sigma_c c_t$, for the four stellar mass bins studied in Section 6.6.1, from low (M1) to high (M4) stellar mass. Note the smaller extent of the horizontal axis compared to other similar figures.

As is customary in galaxy-galaxy lensing studies (and similarly in cluster lensing studies), Hoekstra et al. (2015) ignored the additive bias in Equation 6.11 because the azimuthal averaging of source shapes washes out any spatial anisotropy (in other words, additive biases in γ_1 and γ_2 vanish when projected into γ_t). However, unlike the case of cluster lensing, our measurements are focused on the immediate surroundings of thousands of lenses, such that galaxy light may bias the shape measurements of fainter background sources. Given that the light profile always decreases radially, the azimuthal averaging can introduce an additive bias in γ_t (as opposed to $\gamma_{1,2}$). In Section 6.A we show, using the image simulations described above, that we can model this (negative) bias, c_t, as a function of lens-source separation, lens magnitude and size, and we correct each source's shape measurement for this bias. For reference, a fraction of order 10^{-6} lens-source pairs have $|c_t| > 0.01$.

For illustration, we show in Figure 6.5 the average $c_{\Delta\Sigma} \equiv \Sigma_c c_t$ obtained for real galaxies binned into four stellar mass bins (see Section 6.6.1). As expected, the correction is larger for more massive galaxies, which are on average larger.

6.4.1.1. Sensitivity to background subtraction

The shape measurement algorithm proceeds in two steps. The first is to detect sources using a global background measurement, while the second is to measure the shapes of these detected objects. In the second step, a local background is determined by measuring the brightness in an annulus with inner and outer radii of 16 and 32 pixels, with all detected galaxies masked. This annulus is split into four quadrants and the background is subtracted by fitting a plane through them. This background subtraction works well in general, but in some cases, the background subtraction significantly modifies the estimated magnitude of the test galaxy. Since the simulations do not have a diffuse background component, a proper background subtraction would leave the galaxy magnitude untouched. Therefore changes in the magnitude pre- and post-background subtraction, which we denote δm_{phot},

suggest that the shape measurement process is not robust for that particular galaxy. The simulations indeed contain a population of sources with large values of $\delta m_{\rm phot}$. We discard all source galaxies that meet the following criteria:

$$\begin{aligned} &\delta m_{\rm phot} > 0.0607 + 0.0363 m_{\rm phot} - 0.0152 m_{\rm phot}^2 + 0.0053 m_{\rm phot}^3, \\ &\quad \text{or} \\ &\delta m_{\rm phot} < -0.1607 - 0.0363 m_{\rm phot} + 0.0152 m_{\rm phot}^2 - 0.0053 m_{\rm phot}^3, \end{aligned} \tag{6.12}$$

which represent the edges of the distribution of $\delta m_{\rm phot}$, after accounting for the spread as a function of $m_{\rm phot}$ that arises due to measurement noise. Inspecting the location of the galaxies thus discarded in the real data, we find that they are mostly located either near bright, saturated stars (which have been discarded in previous steps by masking stellar spikes and ghosts), or close to big galaxies with resolved spiral arms or other similar features, that make the plane approximation of the background a very bad fit of the local background. Equation 6.12 therefore effectively acts as a step to identify blended objects. We have verified that the calibration of the shape measurements by Hoekstra et al. (2015) remains unchanged when discarding these galaxies (which were included in their sample). Typically, an additional 10–12 % of sources are masked by Equation 6.12.

6.4.2. Obscuration and contamination by cluster members

Lens galaxies affect the number of detected objects in their vicinity for two reasons: big lenses act as masks on the background source population, while small ones enter the source sample. We refer to these effects as obscuration and contamination, respectively. Since cluster galaxies are randomly oriented (see **Chapter 4**), contamination by cluster members dilutes the recovered lensing signal. Obscuration, in turn, has two effects: it reduces the statistical power of small-scale measurements, and it complicates the determination of contamination, since number density of sources is also affected by it. We resort to the image simulations described above to assess these two effects.

Figure 6.6 shows the source densities measured in the data (i.e., Figure 6.3 collapsed over the vertical axis) and in the real simulations, as a function of lens-source separation, $\theta_{\rm ls}$. The simulated average source densities have been obtained by performing a weighted sum of the

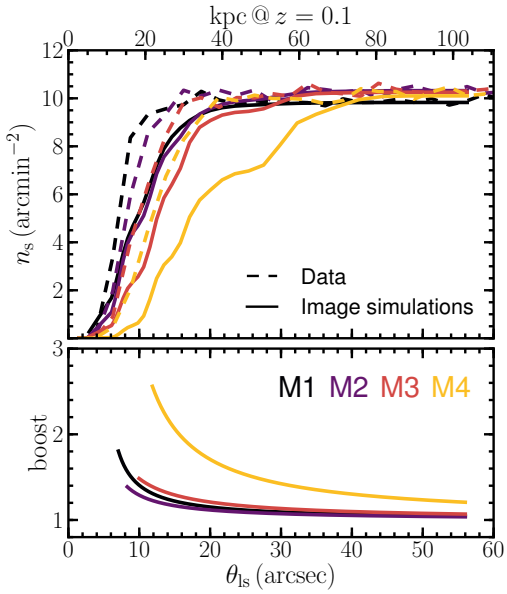

Figure 6.6: Top: average number densities of background sources in the data (dashed) and the image simulations (solid), as a function of lens-source separation, for four bins in stellar mass. The decrease in source density towards $\theta_{\rm ls} = 0$ is produced by obscuration, while the excess density in the data compared to the image simulations corresponds to contamination, by cluster members. Bottom: best-fit boost factors. Lens-source separations below which the source density is less than half of the large-scale value are masked.

source densities measured in simulations with different lens properties. Here, the weights correspond to the number of lenses in the MENeaCS sample with the same magnitude and size of each image simulation setup as per Figure 6.4. Both the data and the simulations show a sharp decrease in the source number density at lens-source separations $\theta_{\rm ls} < 20''$. This decrease effectively means that we have no constraining power below scales $\theta_{\rm ls} \sim 10''$, corresponding to 18 kpc at the median redshift of our sample, $z = 0.1$. This is well beyond the half-light radius of our lenses (see Figure 6.4), and severely limits our ability to constrain the density profile of galaxies at the smallest scales. One possibility to overcome this is to model and subtract lens galaxies from the images to be able to recover a larger source density in the innermost regions; we will explore this in future work.

While both the data and the simulations show a sharp decline in the source density at small scales, the source density profiles are in fact different in an important way. The number density in the image simulations start to decrease at larger scales and do so more slowly than the number densities measured from the data. This difference is produced by cluster members contaminating our source sample, which tends to compensate for the obscuration produced by the lens galaxy on the fainter sources. The bottom panel of Figure 6.6 shows the excess of source galaxies in the real data compared to the simulations, which represents the boost factor defined in Equation 6.10.

Therefore to correct the lensing signal, we repeat the procedure above separately for each considered bin (e.g., in stellar mass). That is, we first generate a two-dimensional histogram of $m_{\rm phot}$ and $\log s_{\rm eff}$ and weight-average the number densities measured in the image simulations. We fit for a boost factor of the form $\mathscr{B}(\theta_{\rm ls}) \propto 1/\theta_{\rm ls}$, which we find provides a good description of the data (shown for the four stellar mass bins in the bottom panel of Figure 6.6). Finally, we average $D_{\rm A}(z)\mathscr{B}(\theta_{\rm ls})$ weighting by the lens distribution to obtain $\mathscr{B}(R)$, and apply the latter to the average $c_{\rm t}$-corrected signal per bin.

Due to lensing, sources are magnified as well as sheared, and this may bias the inferred source number counts discussed in this section, which would have an effect on the boost correction. The increase in flux boosts the number counts relative to an unlensed area of the sky, but the decrease in effective area works in the opposite direction. The net effect depends on the intrinsic distribution of source galaxies as a function of magnitude, and cancels out for a slope $d\log N_{\rm source}/dm_{\rm phot} = 0.40$ (Mellier 1999). In fact, this slope is 0.38–0.40 for the MegaCam r-band data (Hoekstra et al. 2015), so we can safely assume that contamination by cluster members fully explains the excess $n_{\rm s}$ seen in Figure 6.6.

6.4.3. Resulting lensing signal

Figure 6.7 shows the resulting lensing signal from satellites in MENeaCS clusters, corrected by both $c_{\rm t}(\theta_{\rm ls})$ and $\mathscr{B}(R)$. We make the distinction in the arguments of both corrections because the former is applied to each lens-source pair, while the latter is applied as an average correction after stacking all lenses in each bin. We compare the ESDs of the four bins in satellite stellar mass for the spec and spec+RS samples. The signals from the two samples are consistent at the scales where the subhalo dominates, $R \lesssim 100\,{\rm kpc}$. In more detail, the signal from the spec+RS sample is slightly lower than the signal from the spec sample at the smallest scales. This is expected, as in general the more massive galaxies

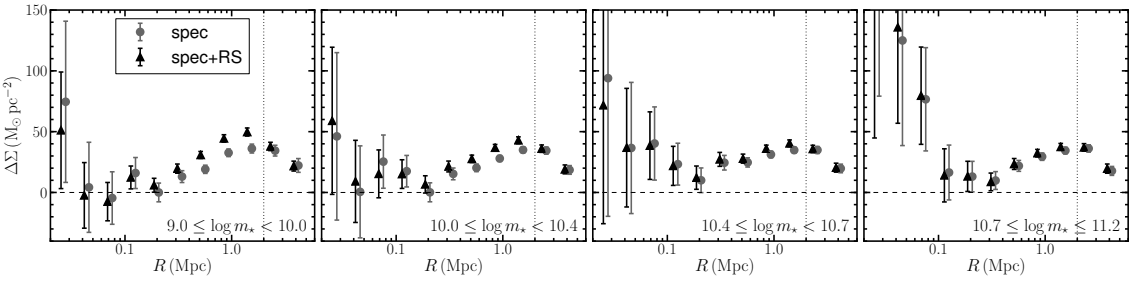

Figure 6.7: Excess surface mass density (ESD) of satellite galaxies binned by stellar mass. Grey circles and black triangles show the ESD of the spectroscopic and spectroscopic-plus-red sequence samples, respectively. Errorbars are the square roots of the diagonal terms of the covariance matrix. The dashed horizontal line shows $\Delta\Sigma = 0$ for reference. In our analysis we only use data points up to 2 Mpc, marked by the vertical dotted line.

have been targeted in the spectroscopic observations; this is reflected also in the average stellar masses listed in Table 6.1. We base our analysis is on the spec+RS sample, which contains a larger sample of lenses.

At intermediate scales, $0.3 \lesssim R/\mathrm{Mpc} \lesssim 2$, the two samples produce different signals. In particular, the signal from the spec+RS sample is higher. This is a consequence of the fact that we only include red sequence galaxies out to 1 Mpc, so the spec+RS sample is on average closer to the cluster centre than the spec sample. Therefore, the peak of the host cluster signal happens at smaller R. Beyond the peak the two signals are consistent, because all galaxies come from the same clusters. See Figure 5.3 for a graphical representation.

6.5. Satellite galaxy-galaxy lensing model

We interpret the galaxy-galaxy lensing signal produced by subhaloes following the formalism introduced by Yang et al. (2006, see also Li et al. 2013a), and applied to observations by Li et al. (2014, 2016) and in **Chapter 5**. This formalism assumes that measurements are averages over a large number of satellites *and* clusters, such that the stacked cluster is (to a sufficient approximation) point-symmetric around their centres and well-described by a given parametrization of the density profile. A similar method was introduced by Pastor Mira et al. (2011), which however does not rely on such parametrization by virtue of subtracting the signal at the opposite point in the host cluster. A different approach is to perform a maximum likelihood reconstruction of the lensing potential of cluster galaxies accounting for the cluster potential, which must be well known a priori (e.g., Natarajan & Kneib 1997; Geiger & Schneider 1998) or modelled simultaneously with the cluster galaxies (Limousin et al. 2005). This method has been applied in several observational studies (e.g., Natarajan et al. 1998, 2009; Limousin et al. 2007). By nature, however, this maximum likelihood approach is well-suited for studies of galaxies in single, rather than stacked, clusters. We discuss results from the literature using either method after presenting our analysis, in Section 6.6. In the following we describe our modelling of the satellite galaxy-galaxy lensing signal.

The ESD measured around a satellite galaxy is a combination of the contributions from the subhalo (including the galaxy itself) at small scales, and that from the host halo at

larger scales,

$$\Delta\Sigma_{\rm sat}(R) = \Delta\Sigma_{\star}(R|m_{\star}) + \Delta\Sigma_{\rm sub}(R|m_{\rm bg}, c_{\rm sub}) + \Delta\Sigma_{\rm host}(R|M_{\rm h}, c_{\rm h}), \tag{6.13}$$

where $\Delta\Sigma_{\star}$ represents the contribution from baryons in the satellite galaxy, which we model as a point source contribution throughout, such that

$$\Delta\Sigma_{\star}(R|m_{\star}) = \frac{m_{\star}}{\pi R^2}. \tag{6.14}$$

Here, we take $m_{\star}$ to be the median stellar mass of all satellites in the corresponding sample (e.g., a given bin in satellite luminosity). In Equation 6.13, R refers to the lens-source separation in physical units; $m_{\rm bg}$ is the average subhalo mass (see below) and $c_{\rm sub}$ its concentration; and $M_{\rm h}$ and $c_{\rm h}$ are the average mass and concentration of the host clusters. In the remainder of this section we describe the other two components in Equation 6.13. Detailed, graphical descriptions of these components can be found in Yang et al. (2006), Li et al. (2013a) and **Chapter 5**.

6.5.1. Host cluster contribution

Numerical simulations reveal that the density profiles of dark matter haloes are well described by a Navarro-Frenk-White (NFW, Navarro et al. 1995) profile,

$$\rho_{\rm NFW}(r) = \frac{\delta_c \rho_{\rm m}}{r/r_{\rm s}\,(1 + r/r_{\rm s})^2}, \tag{6.15}$$

where $\rho_{\rm m}(z) = 3H_0^2(1+z)^3\Omega_{\rm m}/(8\pi G)$ is the mean density of the Universe at redshift z and

$$\delta_c = \frac{200}{3}\frac{c^3}{\ln(1+c) - c/(1+c)}. \tag{6.16}$$

The two free parameters, $r_{\rm s}$ and $c \equiv r_{200}/r_{\rm s}$, are the scale radius and concentration of the profile, respectively. Stacked weak lensing measurements have shown that this theoretical profile is a good description, on average, of real galaxy clusters as well (Oguri et al. 2012; Umetsu et al. 2016). We therefore adopt this parametrization for the density profile of the host clusters.

The concentration parameter is typically anti-correlated with mass. This relation, referred to as $c(M)$ hereafter, has been the subject of several studies (e.g., Bullock et al. 2001; Duffy et al. 2008; Macciò et al. 2008; Prada et al. 2012; Dutton & Macciò 2014). Most of these studies parametrize the $c(M)$ relation as a power law with mass (and some with redshift as well), with the mass dependence being typically very weak. Since our sample covers relatively narrow ranges in both quantities (i.e., cluster mass and redshift), the exact function adopted is of relatively little importance. We therefore parametrize the mass-concentration relation as a power law with mass,

$$c_{\rm h}(M_{200,\rm h}) = a_{\rm c}\left(\frac{M_{200,\rm h}}{10^{15}{\rm M}_{\odot}}\right)^{b_{\rm c}} \tag{6.17}$$

where $M_{200,\rm h}$ is the host halo mass within $r_{200,\rm h}$, and $a_{\rm c}$ and $b_{\rm c}$ are free parameters that we marginalize over. As in **Chapter 5**, we account for the observed separations between the satellites and the cluster centre (which we assume to coincide with the BCG) in each observable bin to model the total host halo contribution to Equation 6.13.

6.5.2. Subhalo contribution

Although in numerical simulations satellite galaxies are heavily stripped by their host cluster, the effect on their density profile is not well established. For instance, Hayashi et al. (2003) found that, although tidal stripping removes mass in an outside-in fashion, tidal heating causes the subhalo to expand; the resulting density profile is similar in shape to that of a central galaxy (which has not been subject to tidal stripping). Similarly, Pastor Mira et al. (2011) found that the NFW profile is a better fit than truncated profiles for subhaloes in the Millenium Simulation (Springel et al. 2005), and that the reduction in mass produced by tidal stripping is reflected only as an overall decrease in the amplitude of the density profiles of subhaloes accreted earlier.

We therefore assume that the density profile of subhaloes can also be described by an NFW profile. However, we adopt the subhalo mass-concentration relation recently derived by Moliné et al. (2016), which depends on both the subhalo mass and its position within the halo,

$$c_{\rm sub}(m_{200}, x) = c_0 \left(1 + \sum_{i=1}^{3} \left[a_i \log\left(\frac{m_{200}}{10^8\, h^{-1}{\rm M}_\odot}\right)\right]^i\right) \times \left[1 + b \log x\right], \tag{6.18}$$

where $x \equiv r_{\rm sat}/r_{\rm h,200}$ (defined in three-dimensional space), $c_0 = 19.9$, $a_i = \{-0.195, 0.089, 0.089\}$ and $b = -0.54$.

Note that the quantity m_{200} is used for mathematical convenience only, but is not well defined physically. Instead, we report subhalo masses within the radius at which the subhalo density matches the background density of the cluster at the distance of the subhalo in question (which we denote $r_{\rm bg}$), and refer to this mass simply as m. This radius $r_{\rm bg}$ scales roughly with cluster-centric distance as $r_{\rm bg} \propto (R_{\rm sat}/r_{\rm 200,h})^{2/3}$ (see also Natarajan et al. 2007, for a comparison between m and m_{200}). The reported subhalo masses are therefore similar to those that would be measured by a subhalo finder based on local overdensities such as SUBFIND (Springel et al. 2001a).

Because the density profile is a steep function of cluster-centric distance, we take the most probable three-dimensional cluster-centric distance, $\langle r_{\rm sat}\rangle$, to be equal to the weighted average of the histogram of two-dimensional distances, $R_{\rm sat}$:

$$\langle r_{\rm sat}\rangle = \frac{\sum_i n(R_{{\rm sat},i}) R_{{\rm sat},i}}{\sum_i n(R_{{\rm sat},i})}, \tag{6.19}$$

where the index i runs over bins of width $\Delta R_{\rm sat} = 0.1\,{\rm Mpc}$ (see Figure 6.2).

6.5.3. Fitting procedure

We fit the model presented above to the data using the affine-invariant Markov Chain Monte Carlo (MCMC) ensemble sampler EMCEE (Foreman-Mackey et al. 2013). This sampler uses a number of walkers (set here to 5000) which move through parameter space depending on the position of all other walkers at a particular step, using a Metropolis Hastings acceptance criterion (see Goodman & Weare 2010, for a detailed description). The loss function to be maximized is defined as

$$\mathscr{L} = \frac{1}{(2\pi)^{k^2/2}} \prod_{m=1}^{k} \prod_{n=1}^{k} \frac{1}{\sqrt{\det(C_{mn})}} \times \exp\left[-\frac{1}{2} (\mathbf{O}-\mathbf{E})_m^T C_{mn}^{-1} (\mathbf{O}-\mathbf{E})_n\right], \tag{6.20}$$

where $k = 4$ is the number of bins into which the sample is split (i.e., stellar mass or cluster-centric distance bins); $\mathbf{O}$ and $\mathbf{E}$ are the observation data vector and the corresponding model predictions, respectively; C is the covariance matrix; $\det(\cdot)$ is the determinant operator; and the index pair (i, j) runs over data points in each bin (m, n). As implied by Equation 6.20, we account for the full covariance matrix, including the covariance both within and between observable bins.

We adopt flat priors for all parameters. For subhalo and host halo masses, the priors are non-zero over the ranges $10^7 \leq m/\mathrm{M}_\odot \leq 10^{15}$ and $10^{13} \leq M_\mathrm{h}/\mathrm{M}_\odot \leq 10^{16}$, respectively. We also adopt flat priors for the parameters characterizing the host density profile, in the ranges $0 \leq a_\mathrm{c} \leq 10$ and $-1 \leq b_\mathrm{c} \leq 1$.

6.6. The connection between mass and light in satellite galaxies

6.6.1. The subhalo-to-stellar mass relation

We first bin the sample by stellar mass, as shown in the top-left panel of Figure 6.2. The ESD of the four bins, along with the model fit, are shown in Figure 6.8. The model is a good description of the data. For reference, this model has $\chi^2 = 14.0$. Since there are 36 data points and 9 free parameters, there are nominally 26 degrees of freedom, but we caution that 'degrees of freedom' is ill-defined for nonlinear models with covariant data points (Andrae et al. 2010), so the interpretation of the χ^2 statistic is not straightforward. The best-fit masses resulting from this model are shown in Figure 6.9. We fit a power law relation between subhalo and stellar masses using the BCES $X_2|X_1$ estimator (Akritas & Bershady 1996), and find a sub-linear relation,

$$\frac{m_\mathrm{bg}}{\mathrm{M}_\odot} = 10^{11.89\pm0.07} \left(\frac{m_\star}{2 \times 10^{10} \mathrm{M}_\odot} \right)^{0.77\pm0.11} . \tag{6.21}$$

We remind the reader that this relation applies to the subhalo mass, m_bg, within the radius r_bg where the subhalo density equals the host halo background density. If we replace m_bg with m_{200}, the normalization increases by a factor 2.45 but the best-fit slope is indistinguishable from that reported in Equation 6.21.

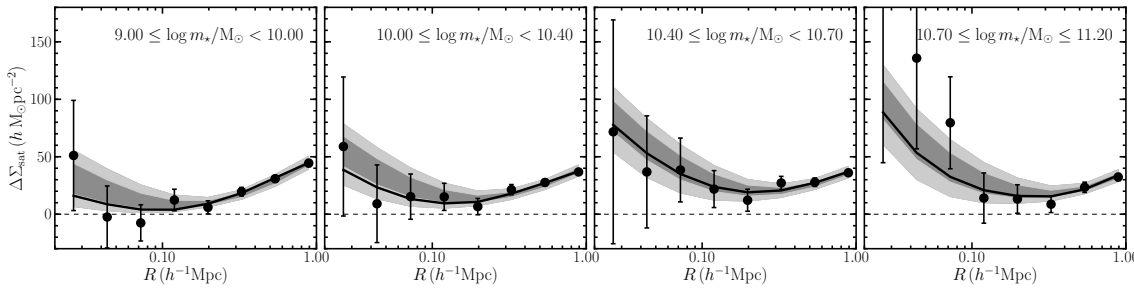

Figure 6.8: Excess surface mass density of the spec+RS sample, binned by stellar mass as shown in the legends (same as the black triangles in Figure 6.7). The black line shows the best-fitting model from the MCMC and the dark and light grey regions show the 68 and 95% credible intervals, respectively. The horizontal dashed line shows $\Delta\Sigma = 0$ for reference.

Table 6.1: Average properties of stellar mass and cluster-centric distance bins used in Sections 6.6.1 and 6.6.2. Each column corresponds to the values of the fiducial spectroscopic-plus-red-sequence sample, the sample of galaxies (both spectroscopic and red sequence) that have a stellar mass measurement, and the spectroscopic-only sample (with and without stellar mass measurements). Note that the 'with-$m_\star$' columns reflect the number of clusters that have three- or four-band photometry, as opposed to those that have only two. See Section 6.3.1 for details on these samples.

Binning observable	Bin label	Range	$N_{\rm sat}$			$\langle R_{\rm sat}/{\rm Mpc}\rangle$			$\log\langle m_\star/{\rm M}_\odot\rangle$		
			spec+RS	with-$m_\star$	spec	spec+RS	with-$m_\star$	spec	spec+RS	with-$m_\star$	spec
$\log(m_\star/{\rm M}_\odot)$	M1	[9.0 – 10.0)	4199	1546	1756	0.69	0.71	0.92	9.59	9.60	9.64
	M2	[10.0 – 10.4)	2501	1591	1742	0.80	0.81	0.93	10.19	10.20	10.20
	M3	[10.4 – 10.7)	1396	1035	1105	0.84	0.86	0.93	10.54	10.54	10.54
	M4	[10.7 – 11.2]	963	737	811	0.88	0.92	0.94	10.88	10.87	10.88
$R_{\rm sat}$ (Mpc)	D1	[0.05 – 0.40)	2509	2021	1044	0.24	0.24	0.24	9.94	9.94	10.14
	D2	[0.40 – 0.70)	2433	1989	1145	0.55	0.55	0.55	9.93	9.94	10.16
	D3	[0.70 – 1.20)	2817	2358	1633	0.90	0.91	0.94	9.96	9.97	10.16
	D4	[1.20 – 2.00]	1821	1655	1818	1.57	1.57	1.57	10.17	10.17	10.17

Table 6.2: Marginalized posterior estimates of fits to the satellite lensing signal. Masses are in units of $\mathrm{M}_\odot$. Uncertainties correspond to 68% credible intervals. All parameters have flat priors, in the following ranges: $10^7 \leq m_{\rm bg}/{\rm M}_\odot \leq 10^{15}$, $10^{13} \leq M_{\rm h}/{\rm M}_\odot \leq 10^{16}$, $0 \leq a_{\rm c} \leq 10$ and $-1 \leq b_{\rm c} \leq 1$.

Observable	$\log\langle m_1\rangle$	$\log\langle m_2\rangle$	$\log\langle m_3\rangle$	$\log\langle m_4\rangle$	$a_{\rm c}$	$b_{\rm c}$	$\log\langle M_{\rm h,1}\rangle$	$\log\langle M_{\rm h,2}\rangle$	$\log\langle M_{\rm h,3}\rangle$	$\log\langle M_{\rm h,4}\rangle$
$m_\star$	$11.17^{+0.31}_{-0.47}$	$11.69^{+0.23}_{-0.32}$	$12.10^{+0.18}_{-0.23}$	$12.06^{+0.22}_{-0.30}$	$4.8^{+1.0}_{-1.2}$	$-0.73^{+0.38}_{-0.16}$	$15.33^{+0.30}_{-0.23}$	$15.23^{+0.34}_{-0.20}$	$15.39^{+0.32}_{-0.25}$	$15.54^{+0.29}_{-0.29}$
$R_{\rm sat}$	$11.07^{+0.30}_{-0.45}$	$11.36^{+0.26}_{-0.37}$	$11.55^{+0.28}_{-0.39}$	$11.59^{+0.31}_{-0.46}$	$3.8^{+1.5}_{-1.5}$	$-0.13^{+0.27}_{-0.26}$	$15.20^{+0.27}_{-0.33}$	$15.88^{+0.09}_{-0.17}$	$15.60^{+0.30}_{-0.53}$	$15.69^{+0.23}_{-0.48}$

We also assess the robustness of the SHSMR to the parametrization of the $c(M)$ relation by adopting that of Duffy et al. (2008) instead of that of Moliné et al. (2016). The slope of the SHSMR is 0.75 ± 0.07, fully consistent with Equation 6.21. However, subhalo masses are then on average $(81 \pm 12)\%$ of those shown in Figure 6.9. Therefore while subhalo masses are somewhat dependent on the adopted $c(M)$ relation, the slope of the SHSMR is insensitive to it.

Rodríguez-Puebla et al. (2013) combined galaxy clustering measurements and abundance matching predictions to obtain the SHSMR[5] in galaxy groups, separating centrals from satellites a priori using the galaxy spectroscopic group catalogue of Yang et al. (2007). As shown in Figure 6.9, their results differ substantially from our measurements, underestimating the subhalo mass by almost an order of magnitude at approximately the pivot stellar mass $m_\star \sim 2 \times 10^{10}\,\mathrm{M}_\odot$. It may be that this difference arises because of the different halo masses probed in both works. To get a sense of this effect, we use the fact that the subhalo mass function, $n(m|M_\mathrm{h})$, depends on host halo mass such that the *normalized* subhalo mass function, $n(m/M_\mathrm{h})$ is universal, and the slope of the SHSMR quoted in Equation 6.21. The groups used by Rodríguez-Puebla et al. (2013) have typical masses slightly above $M_\mathrm{h} = 10^{13}\,\mathrm{M}_\odot$ (Yang et al. 2007), so the average subhalo could be up to 50 times more massive in the MENeaCS clusters. On the other hand, the SHSMR has a slope ~ 0.8, so we estimate "corrected" stellar masses through $m_{\star,1}/m_{\star,0} = (m_1/m_0)^{0.8} = 50^{0.8} \approx 23$ (where subscripts "0" and "1" refer to the original and adjusted masses, respectively). Therefore, the SHSMR should be increased by a factor $50/23 \approx 2.2$. As shown by the thin brown line in Figure 6.9, this correction significantly reduces the difference, and brings the results of Rodríguez-Puebla et al. (2013) in excellent agreement with measurements in EAGLE. (Note that EAGLE probes halo masses $M_\mathrm{h} \sim 10^{14}\,\mathrm{M}_\odot$, so the same argument would push the EAGLE SHSMR up by a factor 1.4.) Of course, this correction is inaccurate, and only meant to give a rough idea of the effect of halo mass. In particular, the correction assumes a constant slope for $m(m_\star)$ over the full stellar mass range, which is obviously not the case for the SHSMR of Rodríguez-Puebla et al. (2013).

We also show in Figure 6.9 various determinations of the stellar-to-halo mass relation (SHMR) of central galaxies from the literature (Leauthaud et al. 2012; Velander et al. 2014; Mandelbaum et al. 2016; van Uitert et al. 2016), where halo mass refers to $M_{200,\mathrm{h}}$.[6] These have all been determined with weak lensing measurements, and are broadly consistent with each other. Both Velander et al. (2014) and Mandelbaum et al. (2016) divided their samples into red and blue centrals, and we only show the results for red galaxies since MENeaCS satellites are in their great majority red as well (see van der Burg et al. 2015).

The comparison between the central SHMR and the satellite SHSMR is however not straightforward. In principle, we may consider in the case of central galaxies that $M_\mathrm{bg} = M_{200,\mathrm{h}}$, so at least the mass definitions are consistent. Even then, identifying the progenitors of present-day satellites is not an easy task, as there is evidence that most satellites in massive clusters today were part of smaller groups long before entering their current hosts. In the context of the decreased star formation of satellite galaxies, this is usually referred

[5] Rodríguez-Puebla et al. (2013) used their measurements to fit for $m_\star(m)$, which due to intrinsic scatter cannot be directly inverted to obtain $m(m_\star)$. Instead, we invert it by Monte Carlo-sampling their relation, including intrinsic scatter, and binning the data points by $m_\star$.

[6] We scale all these relations to the value of H_0 adopted in this work.

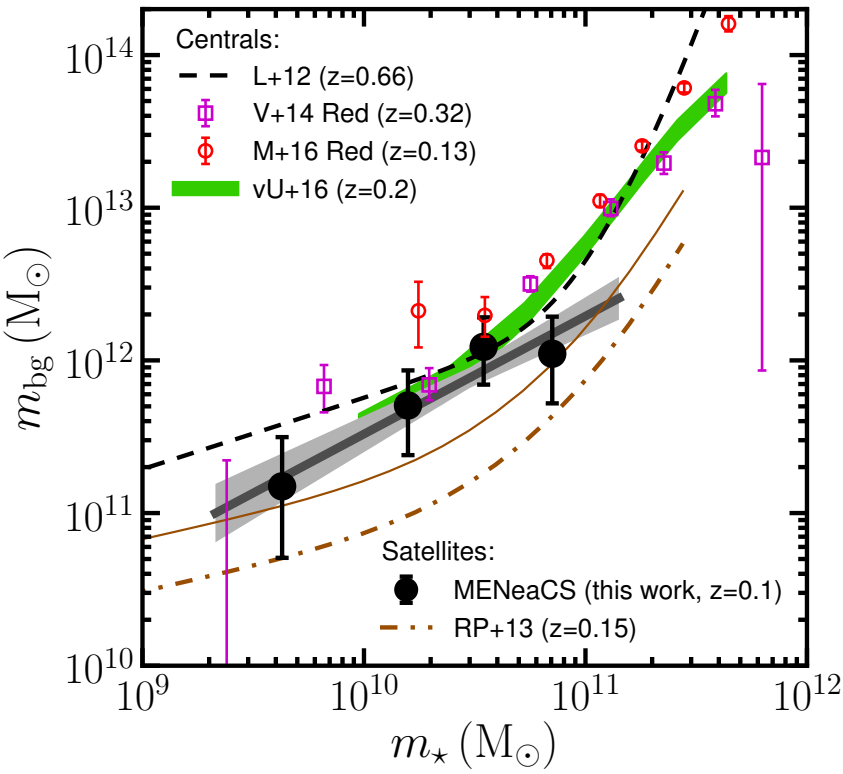

Figure 6.9: Stellar-to-subhalo mass relation. Black circles correspond to the best-fit subhalo masses of spectroscopic plus red sequence satellites, assuming the subhalo mass-concentration relation of Moliné et al. (2016). The grey line and shaded regions show the best-fit linear relation using the BCES $X_2|X_1$ estimator and the 68% confidence interval on the fit, respectively. Subhalo masses refer to the mass within $r_{\rm bg}$ (see Section 6.5.2). We show for comparison the subhalo-to-stellar mass relation of satellites in galaxy groups derived from clustering measurements applied to abundance matching by Rodríguez-Puebla et al. (2013), and the stellar-to-halo mass relations (where halo mass refers to $M_{200,\rm h}$) of central galaxies from galaxy-galaxy lensing measurements by Leauthaud et al. (2012) and van Uitert et al. (2016) and specifically of *red* central galaxies by Velander et al. (2014) and Mandelbaum et al. (2016). The thin brown line shows the SHSMR of Rodríguez-Puebla et al. (2013) boosted by a factor 2.2 to illustrate the effect of the different halo masses of groups used in that work.

to as 'pre-processing' (e.g., McGee et al. 2009; Gabor & Davé 2015; Haines et al. 2015). The impact of this pre-processing on the total mass content of present-day satellites is not known.

The SHMR of central galaxies, like that of satellite galaxies derived by Rodríguez-Puebla et al. (2013), follows a broken power law, with a transition stellar mass of approximately $5\times10^{10}\,\mathrm{M}_\odot$. Given the few data points and the limited range in stellar mass covered here, a double power law fit is not justified, and we cannot place strong constraints on the shape of the SHSMR, beyond noting that a single power law is a good description given the current observational constraints.

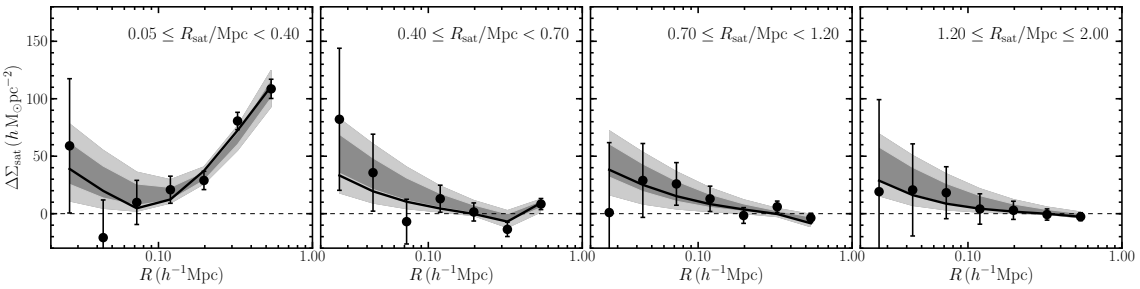

Figure 6.10: Excess surface mass density of satellites binned by cluster-centric distance as shown in the legends. Lines and symbols are the same as Figure 6.8.

6.6.2. Subhalo mass segregation

In this section we explore the dependence of subhalo mass and the ratio between total and stellar masses on the distance to the cluster centre. van den Bosch et al. (2016) have shown using N-body simulations that, even after collapsing the line-of-sight component, the projected halo-centric distance still preserves some of the correlation of subhalo physical parameters with the binding energy, which is closely related to the time a subhalo has spent in the halo. However, after multiple orbits the correlation is significantly reduced because at any particular (projected) distance from the halo centre there are subhaloes with a wide range of infall times. In an average sense, therefore, binning by cluster-centric distance, $R_{\rm sat}$, is binning by time since infall (although with very large uncertainties on the binning quantity). We might therefore expect satellites at similar $R_{\rm sat}$ to have been part of a similar halo-subhalo interaction. Hence the reason to bin by $R_{\rm sat}$ is to test whether we can infer a different degree of transformation for subhaloes in different bins.

Figure 6.10 shows the measured ESD and best-fit model when we split the satellite sample into four $R_{\rm sat}$ bins. Because of the finite extent of our data, we cannot draw full circles with large lens-source separations around most lenses, so additive biases do not cancel out. For this reason, in this section we only use measurements out to $R = 0.6$ Mpc. At larger separations the signal is dominated by the host clusters, with little to no contribution from the subhaloes, and we have verified that subhalo masses are not affected by this cut. The best-fit model shown in Figure 6.10 has $\chi^2 = 14.3$ with 17 'nominal' degrees of freedom (see discussion in Section 6.6.1). We also note that when binning by $m_\star$ as in Section 6.6.1, cluster-centric distances are mixed such that these biases effectively cancel out, and therefore large lens-source separations are not significantly affacted by the finite extent of our images.

van den Bosch et al. (2016) have also shown that the parameter that correlates most strongly with both binding energy and halo-centric distance is the ratio $m/m_{\rm acc}$, where $m_{\rm acc}$ is the mass of the subhalo at the time of its accretion onto the main halo. This is because of the average relation between time a subhalo has spent in the host halo (or the accretion redshift, for a given redshift of observation) and the subhalo's distance to the halo centre, combined with the strong dependence of the mass ratio to the time since accretion as a result of tidal stripping.

We show the ratio of total (subhalo) mass to (galaxy) stellar mass as a function of

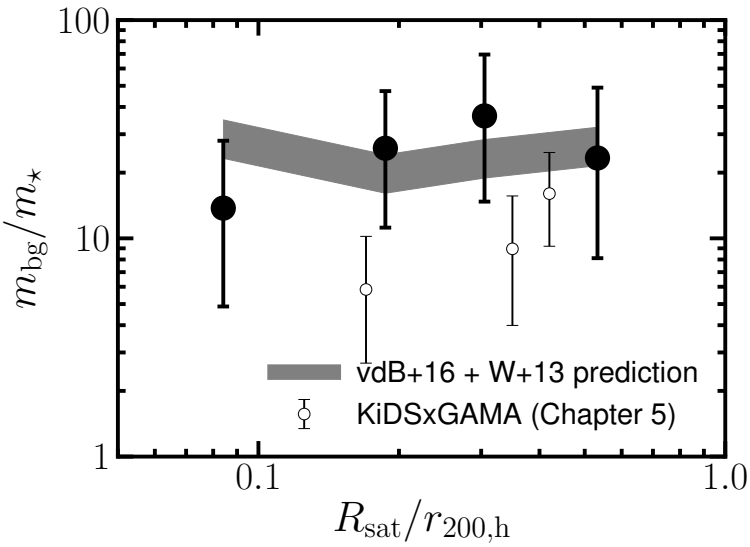

Figure 6.11: Best-fit subhalo-to-stellar mass ratio as a function of projected distance to the cluster centre, in units of the best-fit r_{200} of the host cluster. Small open circles show the results of **Chapter 5** for satellites in galaxy groups. Uncertainties show 68% credible intervals. As in Figure 6.9, all subhalo masses refer to the mass within $r_{\rm bg}$. The grey band shows a prediction for the total-to-stellar mass ratio from numerical simulations from van den Bosch et al. (2016), which give $m/m_{\rm acc}$ as a function of cluster-centric distance, combined with the $m_{\rm acc}(m_\star)$ predictions from Wang et al. (2013), taking the median stellar masses in each $R_{\rm sat}$ bin (cf. Table 6.1). The width of the grey band shows a 20% uncertainty on the model, adopted for illustration.

cluster-centric distance in Figure 6.11. Consistent with **Chapter 5**, we find no statistically significant evidence for a dependence of $m_{\rm bg}/m_\star$ with $R_{\rm sat}$. The values obtained in **Chapter 5** are also shown for comparison, but note that they have been obtained under different assumptions for the concentration of subhaloes and their spatial extent (cf. Sections 5.3.3 and 6.5.2). To allow a fair comparison (which should nevertheless be taken with caution), we adjust the subhalo masses obtained in **Chapter 5** to be consistent with those reported in this Chapter. In **Chapter 5**, we adopted the mass-concentration relation of Duffy et al. (2008) for the density profiles of subhaloes. Following the discussion of the previous section, we divide the masses reported in **Chapter 5** by 0.81 to correct for the different concentrations. We also calculate $m_{\rm bg}$ for the subhaloes in **Chapter 5**, taking the best-fit host halo masses (cf. Table 5.2) and average group-centric distances (Table 5.1). At $R_{\rm sat} \sim 0.2-0.3\,{\rm Mpc}$, the total-to-stellar mass ratio in galaxy groups derived in **Chapter 5** is marginally smaller (at the $\sim 2\sigma$ level) than that in galaxy clusters derived here. This may point to a host halo mass dependence of the subhalo-to-stellar masses, but a definitive claim requires smaller errorbars.

We also show a prediction from numerical simulations and semi-analytic models. For this, we first use the average $m/m_{\rm acc}$ (where $m_{\rm acc}$ is the subhalo mass at the time of accretion) as a function of projected distance from van den Bosch et al. (2016).[7] We combine

[7] van den Bosch et al. (2016) used subhalo masses obtained by the subhalo finder ROCKSTAR (Behroozi et al. 2013), which uses phase-space information to determine the membership of dark matter particles to a given subhalo, and has been shown to give larger subhalo masses than SUBFIND, especially at low

these predictions with the predictions for $m_{\rm acc}(m_\star)$ from Wang et al. (2013), assuming four different values for the stellar masses, given by the median masses for each bin quoted in Table 6.1, including a 20% uncertainty for illustration.[8] These predictions are in good agreement with our measurements, and show that we do not expect to see a trend with cluster-centric distance even when normalizing by stellar mass, if the stellar masses increase with $R_{\rm sat}$, as in our case (cf. Table 6.1 and Figure 6.2). Furthermore, any segregation at fixed stellar mass is too mild to be detected with current uncertainties. Several previous observational studies have focused on the mass segregation of subhaloes. However, differences in the adopted density profiles, mass definitions, and the fact that some works did not report the masses of the host clusters (nor normalized cluster-centric distance by host cluster size), preclude a detailed comparison with our results. To contextualize our results, we nevertheless compare these studies to the present one in a qualitative sense.

Using galaxy-galaxy lensing measurements of subhaloes in redMaPPer clusters (which have an average mass $M_{\rm h} \sim 10^{14}\,{\rm M}_\odot$; Rykoff et al. 2014), Li et al. (2016) found that the subhalo-to-stellar mass ratio increases by an order of magnitude from $R_{\rm sat} \sim 0.2\,{\rm Mpc}$ to $R_{\rm sat} \sim 1\,{\rm Mpc}$, when assuming a truncated NFW density profile, marginalizing over both the truncation radius and the concentration. Their trend with projected distance is stronger than that found here and than that predicted by N-body simulations and semi-analytical models (Han et al. 2016, see also Figure 6.11). As hinted by the comparison of the present results with **Chapter 5**, this may be due to a dependence of the mass segregation on the mass of the host cluster, but again we note that the uncertainties in both our studies and in Li et al. (2016) also allow for both no segregation and no dependence on cluster mass. Interestingly, Roberts et al. (2015) found a strong dependence of the segregation of *stellar* mass on host cluster mass, such that galaxies in more massive clusters are not segregated. Note that the segregation in stellar mass measured by Roberts et al. (2015) is, as expected, opposite that suggested by Li et al. (2016) for the total-to-stellar mass ratio, because the former is not as prone to tidal stripping as it is to dynamical friction.

Okabe et al. (2014) measured the lensing signal of galaxy- and group-scale subhaloes in the Coma cluster using observations with the Subaru telescope. They found that, while subgroup-scale subhaloes (which they analyzed individually) are better fit by truncated profiles, a stack of individual luminous galaxies is well-fit by a simple NFW model like the one adopted in this work, with no discernible truncation radius. This suggests that, maybe, the stacking of subhaloes with varying truncation radii, produces an average signal in which a truncation radius is no longer discernible, consistent with the findings of Pastor Mira et al. (2011) using the Millenium simulation (Springel et al. 2005). However, this contrasts with the results of Natarajan et al. (1998, 2002, 2007, 2009) and Limousin et al. (2007), who found evidence for galaxy truncation when studying galaxies in a few galaxy clusters at $z = 0.2 - 0.6$. Moreover, these studies found significant evidence for smaller truncation radii (or, equivalently, more compact cores) in galaxies closer to the cluster centres. It is unclear whether the methodology itself allowed the latter set of authors to

halo-centric radii (Knebe et al. 2013). Therefore the comparison between the predictions and observational results in Figure 6.11 should be done with care.

[8] Wang et al. (2013) report the $m_\star(m_{\rm acc})$, which because of intrinsic scatter cannot be directly inverted to obtain $m_{\rm acc}(m_\star)$. Instead, we obtain the latter by sampling the $m_\star(m_{\rm acc})$ relation including intrinsic scatter, and then taking the average $m_{\rm acc}$ when binning by $m_\star$.

detect a truncation radius while our methodology is more limiting in this respect (see Section 6.1 for a discussion of the different formalisms) , or if the parametrization of the subhalo mass density profile has any influence on this discrepancy, as argued by Pastor Mira et al. (2011). We do note that the azimuthal averaging necessarily washes out anisotropic information which is in fact used by the maximum likelihood approach. We have verified that, even if we bin the sample into only two or three bins (rather than four), we still cannot constrain the shape of the density profiles, due to the hard limit imposed by obscuration by cluster members (Section 6.4). Since the papers above do not show the signal from which their results are derived, it is difficult to assess the origin of the different conclusions we reach compared to theirs. The papers by Natarajan et al. used Hubble Space Telescope observations, which opens up that the possibility that a measurement of the density profiles of subhaloes requires data taken from space. However, this is not the case of Limousin et al. (2007), who in fact also used CFHT data for their measurements. As shown in Figure 6.6, the source density drops to roughly 50% at a distance of 20 kpc (at $z = 0.1$) due to obscuration by cluster members. It is therefore unlikely that truncation radii of order 10–20 kpc, as measured by Limousin et al. (2007), can be detected directly with weak lensing measurements using ground-based observations, irrespective of the method employed. Subtracting the light of lens galaxies from the images before the source sample is constructed might improve small-scale measurements; we will explore this in future work.

6.6.3. Host clusters

As discussed in the previous sections, in modelling the satellite lensing signal we must model the contribution from the host halo as well, even if it has little impact on the subhalo masses. However, since our measurements extend at most to $R = 1\,\mathrm{Mpc}$, we cannot break the degeneracy between host mass and concentration. Nevertheless, we list for completeness the best-fit values for the host clusters in Table 6.2. When binning by stellar mass, the best-fit power law for the concentration is significantly steeper than the values $b_c \sim -0.1$ suggested by numerical simulations (e.g., Duffy et al. 2008; Dutton & Macciò 2014), but this is due to the strong degeneracy of the concentration with mass, which pushes the average masses to unrealistically large values. As shown in **Chapter 5**, the mass and concentration of the host clusters produce different changes in the satellite lensing signal, which are easily discernible if the measurements extend beyond the turnover of the host signal (at $R \gtrsim 2\,\mathrm{Mpc}$ for massive clusters). Since this is not our case, our data can accomodate varying values for both concentrations (which change the slope of the increase in signal at intermediate scales) and masses (which reflect as an overall normalization at intermediate to large scales). These uncertainties in the parameters of the density profile of host haloes has no significant impact on the constraints on subhalo masses.

6.7. Conclusions

We present the average masses of satellite galaxies in massive galaxy clusters at $0.05 < z < 0.15$ using weak galaxy-galaxy lensing measurements. We use a combination of deep, high-quality, wide-field observations of galaxy clusters (Sand et al. 2012) and extensive archival spectroscopic data (compiled in **Chapter 4**). Using extensive image simulations

of bright lenses in the foreground of a population of field galaxies resembling the sources in the analysis, we model and account for biases arising from (i) shape measurements, due to confusion of light from the lens with the faint sources, and (ii) contamination of the source sample by faint cluster members (Section 6.4).

We model the lensing signal from subhaloes using an NFW profile and the subhalo mass-concentration relation measured from N-body simulations by Moliné et al. (2016), which depends on cluster-centric distance as well. We split the sample in bins of stellar mass and measure the subhalo-to-stellar mass relation (SHSMR) of galaxies in massive clusters. This is the first measurement of the SHSMR from weak lensing. Fitting the resulting masses with a power-law relation, we find $\log m_{\rm bg} = (11.73 \pm 0.05) + (0.77 \pm 0.11) \log m_{\star}$. The slope of this relation is robust to both the adopted subhalo mass-concentration relation and the subhalo mass definition. The SHSMR is broadly consistent with the corresponding relation for central galaxies, but a more detailed comparison requires the use of simulations.

We also study the masses of subhaloes at different cluster-centric distances with the aim of studying the evolution of subhaloes within clusters. Similar to recent results, we cannot constrain the truncation radii of subhaloes, while previous studies based on a different formalism have claimed significant detections. We also find no statistically significant evidence for mass segregation, consistent with recent results and with predictions from a combination of numerical simulations and semi-analytic models. Although direct comparison with the observational literature is complicated by the use of different definitions and conventions, the results of this chapter are consistent with **Chapter 5**, but most other works have found at least some evidence for mass segregation (e.g., Natarajan et al. 2002; Li et al. 2016). The origin of these discrepancies is not clear, and more work is needed to elucidate it.

Our measurements of mass segregation are broadly consistent with predictions from numerical simulations, while the SHSMR is almost an order of magnitude higher than that inferred from abundance matching applied to galaxy clustering measurements. A more detailed interpretation of our measurements in the context of these predictions requires a detailed analysis of hydrodynamic simulations, where both the satellites and their host haloes can be selected to match the observational situation. With these simulations we

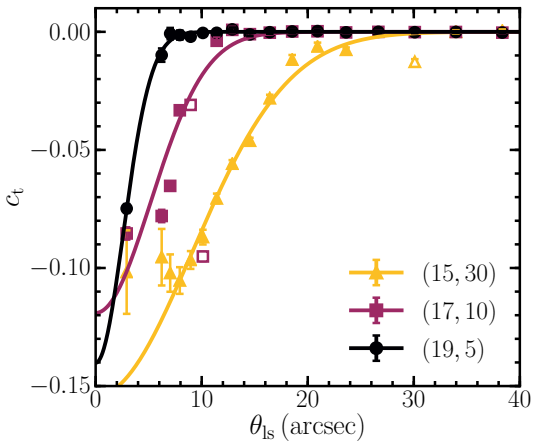

Figure 6.12: Tangential biases measured in three sets of image simulations. The legend shows the magnitude and size (in pixels) of each set. The three examples correspond to big bright (yellow triangles), average (brown squares), and small faint (black circles) simulated lenses, and illustrate the range of biases in our sample. The relevance of each set with respect to the real satellite galaxies can be seen in Figure 6.4. Data points with errorbars show measured tangential shear and solid lines show Gaussian fits to each set of simulations. Empty points are biased because they are adjacent the chosen truncation radius of the lenses, and are excluded from the fits.

would also be able to test some assumptions of our model, most notably the concentration of the subhalo density profile, and reveal the origin of the observed connection between mass and light in cluster galaxies.

6.A. Lens-induced bias on the shape measurements

Extended light from bright lens galaxies affects measurements of sources, such that their shapes are estimated to be more radially elongated than they really are. This induces a negative additive bias *in the coordinate frame of the lens galaxy*, which we label c_t.

In order to account for this bias we measure the shapes of galaxies in the image simulations of Hoekstra et al. (2015), after injecting bright lens galaxies in a grid pattern (separated by 1 arcmin from each other). These injected lenses are modelled as a Sérsic (1968) profile (i.e., $I(r) \propto r^{1/n}$) using GALSIM (Rowe et al. 2015), with a power-law index $n = 4$. Details about the simulated source population can be found in Hoekstra et al. (2015). The image simulations have a constant shear applied to them, which cancels out when we average shape measurements tangentially around the lenses. Therefore any measured shear in the tangential frame can be attributed to a bias induced by extended light from the lenses. The lenses we inject into the simulations span the ranges $14 \leq m_{\rm phot} \leq 20$ and $3 \leq s_{\rm eff}/{\rm pix} \leq 40$ (corresponding to $0.''55 \leq s_{\rm eff} \leq 7.''40$), and are compared to the magnitude and size distribution (as measured with GALFIT in **Chapter 4**) in the MENeaCS data in Figure 6.4.

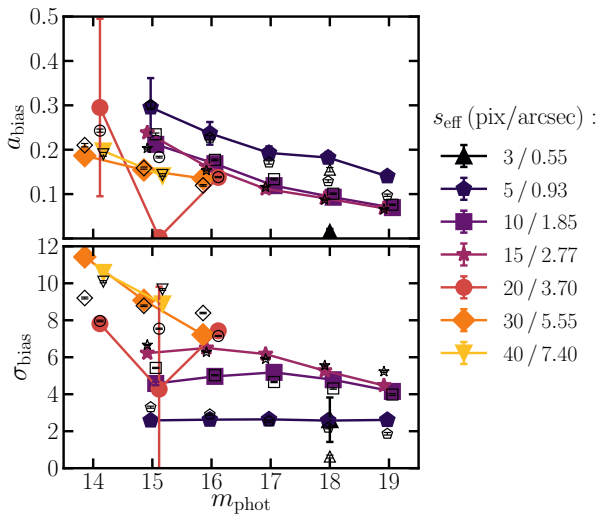

Figure 6.13: Amplitude and width of Gaussian fits to the additive bias c_t (solid symbols), and the results from an overall fit to each panel given in Equation 6.23 (empty symbols). Solid lines connect simulation sets with the same half-light radius as shown in the legend.

We show the measured c_t for three sample sets of simulations in Figure 6.12. We find that the bias profiles can be well modelled in each bin as a Gaussian centred at $\theta_{\rm ls} = 0$,

$$c_t(\theta_{\rm ls}) = a_{\rm bias} \exp\left[\frac{-\theta^2}{2\sigma^2_{\rm bias}}\right]. \tag{6.22}$$

We then fit the best-fit parameters $a_{\rm bias}$ and $\sigma_{\rm bias}$ as functions of lens magnitude and size,

$$\begin{aligned} a_{\rm bias} &= -0.81 - 1.22(m_{\rm phot} - 16) - 0.36\log(s_{\rm eff}/15\,{\rm pix}), \\ \sigma_{\rm bias} &= 6.27 - 14.01\log(m_{\rm phot}/16) + 7.04\log(s_{\rm eff}/15\,{\rm pix}). \end{aligned} \tag{6.23}$$

Figure 6.13 shows the best-fit individual values of $a_{\rm bias}$ and $\sigma_{\rm bias}$ and the values predicted by Equation 6.23. While at face value Equation 6.23 is not a good description of the

measurements in the simulations for the full ($m_{\rm phot}$,$s_{\rm eff}$) space (and especially for $\sigma_{\rm bias}$), the discrepancy is limited to the extremes of this space. One notable discrepancy is roughly a 25% difference in the prediction of $\sigma_{\rm bias}$ for $(m_{\rm phot}, s_{\rm eff}) = (14, 30)$ (here, sizes are given in pixels). However, as shown in Figure 6.4, this combination of magnitude and size accounts for much less than 1% of the lenses in our sample. The other notable difference happens at $(m_{\rm phot}, s_{\rm eff}) = (18, 3)$, but the bias introduced by such small, faint galaxies is negligible to start with. Moreover, as can be seen in Figure 6.13, the difference arises because of the degeneracy between the amplitude and width of the Gaussian, such that the predicted bias is negligible as well.